

Banner appropriate to article type will appear here in typeset article

1 Influence of Electric Potential Decay to the Impact 2 Regimes of Droplets on a Hydrophobic Electrode

3 Ziqiang Ma¹, and Xinping Zhou^{1,2†}

4 ¹School of Mechanical Science and Engineering, Huazhong University of Science and Technology, Wuhan
5 430074, PR China

6 ²State Key Laboratory of Intelligent Manufacturing Equipment and Technology, Huazhong University of
7 Science and Technology, Wuhan 430074, China

8 (Received xx; revised xx; accepted xx)

9 Direct numerical simulations of Popinet (2003)

10 **Key words:** Authors should not enter keywords on the manuscript, as these must be chosen by
11 the author during the online submission process and will then be added during the typesetting
12 process (see [Keyword PDF](#) for the full list). Other classifications will be added at the same
13 time.

14 1. Introduction

15 The dynamics of droplet impact on solid surfaces is a classical problem in fluid mechanics,
16 with various engineering applications, including inkjet printing, spray cooling, and microfluidic
17 actuation. The interaction between inertia, surface tension, viscosity, and wettability
18 gives rise to complex behaviors, such as spreading, retraction, rebound, or splashing. In
19 recent years, the ability to actively modulate wettability through external stimuli has attracted
20 significant interest, particularly via electrowetting-on-dielectric (EWOD). In EWOD systems,
21 the apparent contact angle of a droplet can be dynamically controlled by applying an electric
22 potential across a dielectric-coated electrode, enabling real-time tuning of droplet behavior.

23 Previous studies have extensively investigated the role of electrowetting in modifying
24 contact angle hysteresis, controlling spreading dynamics, and suppressing rebound. Most of
25 these works, however, assume that the applied electric field is spatially uniform. In practical
26 implementations—especially when thin electrodes with finite conductivity or localized voltage
27 sources are employed—the electric potential may decay laterally along the substrate. This non-
28 uniformity can lead to spatial gradients in wettability and contact angle, potentially altering
29 the droplet impact regimes. Despite its physical relevance, the influence of electric potential
30 decay on droplet dynamics has received little attention and remains poorly understood.

31 In this work, we study the impact of a millimetric water droplet on a hydrophobic substrate
32 subject to a laterally decaying electric potential of the form $\phi(r) = \phi_0 e^{-\alpha r}$, where α is
33 the electric potential decay constant. Using a dimensionless formulation, we investigate

† Email address for correspondence: JFMEditorial@cambridge.org

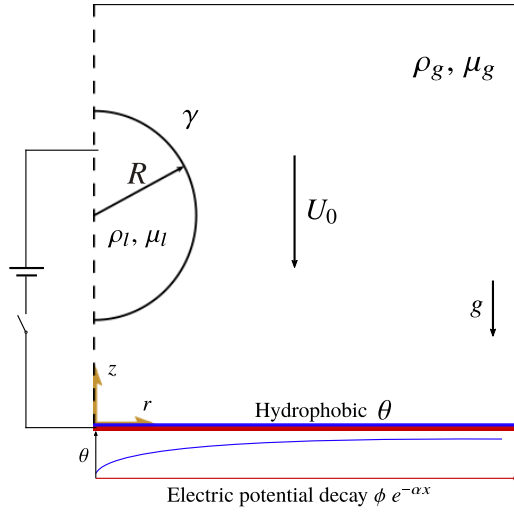


Figure 1: model

34 how this spatial variation in potential affects the contact angle distribution, impact-induced
 35 deformation, and rebound behavior. Furthermore, we extend our analysis to include time-
 36 harmonic potentials to examine the frequency-dependent response of the droplet under
 37 alternating fields. A combination of numerical simulation and phase-space classification is
 38 employed to delineate different behavioral regimes.

39 The paper is organized as follows. Section 2 introduces the problem formulation and
 40 numerical methods. Section 3 presents a phase diagram and classification of electrowetting-
 41 induced wettability. The influence of electric potential decay on droplet dynamics is then
 42 examined, followed by an analysis of the frequency-dependent response of droplet behavior
 43 under time-varying electric potentials. Conclusions are drawn in Section 4.

44 2. Problem and method

45 2.1. Governing equations and numerics models

46 Consider a water droplet of diameter D placed upon the substrate exhibiting electric potential
 47 decay $\phi e^{-\alpha r}$, where α is the electric potential decay constant. The droplet impacts the
 48 electrowetting surface with the velocity U_0 . The density and viscosity are denoted by ρ and
 49 μ , with subscripts l and g indicating the liquid and the surrounding gas. In the electrowetting
 50 on dielectric (EWOD) phenomena under consideration, the wettability of substrate is varied
 51 by applied electric current. The variation of contact angle which is induced by electrowetting
 52 can be described by the Young-Lippmann equation

$$53 \quad \cos(\theta_{ew}) = \cos \theta_s + \frac{\epsilon_0 \epsilon_r}{2 \gamma d} \phi^2. \quad (2.1)$$

54 θ_s is the static contact angle, θ_{ew} is the electrowetting induced contact angle, and γ is
 55 the surface tension. ϵ_0 is the vacuum's permittivity, ϵ_r and d is the dielectric constant and
 56 dielectric thickness. Due to the electric potential decay, the contact angle at the wall exhibits a
 57 trend of being lower at the center and higher at the periphery. Figure 1 shows the configuration
 58 of the water droplet in the domain for computations.

59 The water droplet and surrounding fluid are controlled by the continuity and momentum
 60 equations for the incompressible fluids

61 $\nabla \cdot \mathbf{u} = 0,$ (2.2)

62 $\rho(\partial_t \mathbf{u} + \mathbf{u} \nabla \cdot \mathbf{u}) = -\nabla p + \nabla \cdot \mu(\nabla \mathbf{u} + \nabla^T \mathbf{u}) + \gamma \kappa \delta_s \mathbf{n} + \rho \mathbf{g},$ (2.3)

63 where p is the pressure, \mathbf{g} is the gravity acceleration. A volume fraction function, denoted by
 64 c , is introduced to distinguish between the two immiscible fluid phases in the computational
 65 domain. Specifically, $c = 1$ corresponds to the liquid phase (water), and $c = 0$ corresponds to
 66 the gas phase (air). This function is constructed based on the known location of the interface.
 67 Since the density ρ and viscosity μ are constant within each phase, their spatial distributions
 68 across the domain can be conveniently expressed in terms of c as follows:

69
$$\begin{aligned}\rho &= \rho_g + (\rho_l - \rho_g)c, \\ \mu &= \mu_g + (\mu_l - \mu_g)c,\end{aligned}$$
 (2.4)

70 where subscripts l and g denote the liquid and gas phases, respectively. The function c
 71 thus implicitly tracks the interface and evolves in time according to the following advection
 72 equation:

73 $\partial_t c + \nabla \cdot (c \mathbf{u}) = 0,$ (2.5)

74 We nondimensionalize all variables using the diameter of the drop D . Therefore, the timescale
 75 is $\tau = \sqrt{\rho_l D^3 / \gamma}$, the velocity scale is $\sqrt{\gamma / \rho_l D}$, and the length scale is D . The three
 76 nondimensional parameters, the Ohnesorge number, the Weber number, the Bond number:

77 $Oh = \frac{\mu}{\sqrt{\rho \gamma D}}, We = \frac{\rho D U_0}{\gamma}, Bo = \frac{\rho g D^2}{\gamma}.$ (2.6)

78 We consider the effect of gravity by setting Bo as a constant in all cases. And all the material
 79 properties the density ratio ρ_g / ρ_l , the viscosity ratio μ_g / μ_l are typically defined as constants
 80 1×10^{-3} and 1.79×10^{-2} . Here, a Volume-of-Fluid (VOF) method of combining an adaptive
 81 quad spatial discretisation (Popinet 2003, 2009; Afkhami *et al.* 2009, 2018) is chosen to
 82 implement the electrowetting technique with dynamic contact angle model.

83 When a sessile droplet equilibrium on the substrate, the static contact angle θ_s is the angle
 84 between the interface of droplet and the substrate surface. The dynamic contact angle θ_D is
 85 implemented using the molecular kinetic theory (MKT) (Duvivier *et al.* 2013; Cheng *et al.*
 86 2018; Kumar & Pathak 2024). Using the theory, the dynamic contact angle θ_D and contact
 87 line velocity v_{cl} have the following relationship:

88 $v_{cl} = 2k_s^0 l \left(\frac{h}{\mu V_m} \right) \sinh \left[\frac{\gamma}{2nk_B T} (\cos \theta_s - \cos \theta_D) \right].$ (2.7)

89 The values of all reference parameters employed in the present study are summarized in
 90 Table 1. The contact line velocity is limited by the maximum for the dynamic contact angle
 91 of 180° and the minimum for the dynamic contact angle of 0° :

92 $v_{cl180^\circ} = 2k_s^0 l \left(\frac{h}{\mu V_m} \right) \sinh \left[\frac{\gamma}{2nk_B T} (\cos \theta_s + 1) \right],$ (2.8)

93 $- v_{cl0^\circ} = 2k_s^0 l \left(\frac{h}{\mu V_m} \right) \sinh \left[\frac{\gamma}{2nk_B T} (1 - \cos \theta_s) \right].$ (2.9)

Parameter	Description	Value
ϵ_0	Vacuum permittivity	8.85×10^{-12} m
ϵ_r	Dielectric constant	2.6
k_s^0	Dielectric constant	4.5627×10^{10} s ⁻¹
l	Molecular displacement	5×10^{-10} m
h	Planck constant	6.63×10^{-34} Js
V_m	Molecular volume	3×10^{-29} m ³
k_B	Boltzmann constant	1.38×10^{-23} m ³
T	Temperature	298.15 K
d	Dielectric thickness	1×10^{-5} m

Table 1: Summary of operating parameters used for MKT model in the simulations.

94 Although the contact line velocity v_{cl} , can theoretically exceed both upper and lower limit,
95 the numerical simulations are constrained to operate within the limits specified by Eqs. 2.8
96 and 2.9. Under reference conditions, the dynamic contact angle (DCA) is inferred from the
97 prescribed contact line velocity by inverting the corresponding relation. The expression used
98 to compute the DCA is given by

$$99 \quad \theta_D = \cos^{-1} \left[\cos \theta_s - \left(\frac{2n k_B T}{\gamma} \sinh^{-1} \left(\frac{v_{cl} \mu V_m}{2k_s^0 l h} \right) \right) \right]. \quad (2.10)$$

100 Electrowetting technique enables dynamic control of surface wettability by applying an
101 electric potential across a conductive droplet. When the electric potential is established
102 between the droplet and an underlying electrode, charges accumulate at the three-phase
103 contact line. This localized buildup of electric charge leads to a reduction in the interfacial
104 energy between the droplet and the substrate. The extent of contact angle modulation depends
105 on the properties of the liquid, the characteristics of the substrate, and the parameters of the
106 applied electric field in Eqs. 2.1. Accordingly, the relationship between the dynamic contact
107 angle induced by electrowetting and contact line velocity is described by:

$$108 \quad \theta_{ED} = \cos^{-1} \left[\cos \theta_s + \frac{\epsilon_0 \epsilon_r}{2 \gamma d} \phi^2 - \left(\frac{2n k_B T}{\gamma} \sinh^{-1} \left(\frac{v_{cl} \mu V_m}{2k_s^0 l h} \right) \right) \right]. \quad (2.11)$$

109 2.2. Problem setup and numerics validation

110 As shown in figure 1, a spherical water droplet of diameter D is initially positioned in
111 close proximity to the lower boundary, which consists of a solid substrate subject to an
112 applied electric potential. The droplet impacts the surface with a prescribed velocity U_0 , and
113 the dynamics are governed by the electrowetting-on-dielectric (EWOD) mechanism. Initially,
114 the contact angle is static, with $\theta_s = 90^\circ$. Upon actuation, the contact angle varies dynamically
115 in response to the applied voltage, which is both spatially and temporally dependent. The
116 applied voltage is defined as

$$117 \quad \phi(r, t) = \phi_0 \cos(2\pi f t) \cdot e^{-\alpha r}, \quad (2.12)$$

118 where ϕ_0 is the peak amplitude of electric potential, f is the oscillation frequency, and
119 α characterizes the radial decay of the electric potential, accounting for the influence of a
120 uniform resistance on the potential distribution along the dielectric layer. The computational
121 domain is taken as $8R \times 8R$ to ensure sufficient space for droplet deformation and spreading

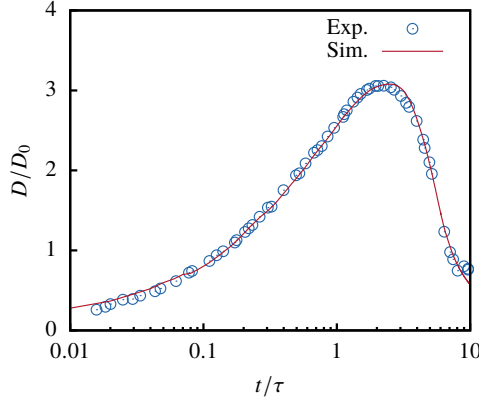


Figure 2: Comparison of drop spreading radius during impact process obtained from experiment data reported by Šikalo *et al.* (2002).

122 during impact and subsequent evolution. The bottom of the computational domain ($z = 0$)
 123 is a no-slip boundary condition, and the left ($r = 0$) is an axisymmetric boundary condition.
 124 All remaining boundaries of the computational domain are open boundary conditions.

125 Building upon earlier incompressible flow theories (Smith *et al.* 2003; Korobkin *et al.*
 126 2008), Mandre *et al.* (2009) derived a criterion to assess the relevance of gas compressibility
 127 during high-velocity droplet impacts. Specifically, they introduced a non-dimensional com-
 128 pressibility parameter defined as the ratio between the ambient atmospheric pressure and a
 129 characteristic lubrication pressure in the gas layer:

$$130 \quad \epsilon = \frac{P_{\text{atm}}}{(0.5 * DU_0^7 \rho_l^4 / \mu_g)^{1/3}}, \quad (2.13)$$

131 where P_{atm} is the ambient atmospheric pressure, and μ_g the gas viscosity. According to their
 132 analysis, gas compressibility becomes significant when $\epsilon^{-1} \gtrsim 3$. In light of this criterion,
 133 and supported by the conclusions of Li & Thoroddsen (2015) and Mandre *et al.* (2009), we
 134 neglect gas compressibility effects in the present study. The estimated range of the inverse
 135 compressibility parameter in our simulations is $\epsilon^{-1} \approx 0.1\text{--}2.0$, which remains well below
 136 the threshold for compressibility to play an important role. These values differ slightly from
 137 those in earlier studies due to variations in Ohnesorge (Oh) and Weber (We) numbers, but
 138 they still justify the assumption of incompressibility for the gas phase under the current
 139 impact conditions.

140 To ensure the accuracy and reliability of the numerical model, simulation results are
 141 validated against experimental data reported by Šikalo *et al.* (2002). Figure 2 presents the time
 142 evolution of the spreading radius of the droplet, normalized by its initial radius, as a function
 143 of the non-dimensional time. All physical parameters used in the simulation are consistent
 144 with those in the referenced experiment. In particular, the Weber number is $We = 44$, and the
 145 static contact angle is set to 100° , matching the experimental configuration. The simulation
 146 results exhibit excellent agreement with the experimental data, thereby demonstrating the
 147 validity of the computational model in capturing the essential physics of droplet impact and
 148 spreading dynamics.

149 For grid independence, we compare the spreading radius with time obtained from
 150 simulations, using different grid resolutions to assess the effect of varying grid sizes
 151 on the simulation accuracy. Figure 3 shows the finest grid sizes from low to high are

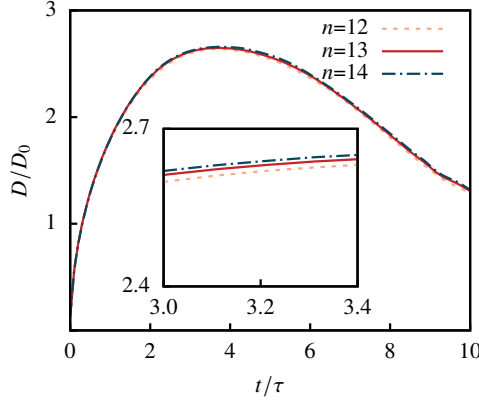


Figure 3: Comparison of drop spreading radius during impact process obtained from simulations at $We = 20$.

152 $\Delta/D = 4.8 \times 10^{-3}$, $\Delta/D = 2.4 \times 10^{-3}$, and $\Delta/D = 1.2 \times 10^{-3}$ for the given computational
 153 domain. The orange dash line is the finest grid level 12, the red line is the finest grid level 13
 154 and the blue dash line is the finest grid 14. Despite these minor differences in the three levels,
 155 we notice that the middle grid size level reach the results are not significantly influenced by
 156 the grid resolution, while also accounting for the prohibitive computational costs involved.
 157 Thus, we choose the middle grid size level for all of our simulations.

158 3. Results

159 In order to compare the dynamics of droplet motion, we first deployed droplets to impact on
 160 substrates with the same initial static contact angle, $\theta_s = 90^\circ$. The droplets go through three
 161 distinct stages: spreading, retracting, and rebounding, before eventually detaching from the
 162 substrate. To actively control the contact angle during these dynamics, a voltage is applied
 163 between the conducting droplet and an underlying insulated electrode. This configuration,
 164 typical of the electrowetting-on-dielectric (EWOD) setup, consists of a hydrophobic dielectric
 165 layer that electrically isolates the droplet from the conductive substrate. When the electric
 166 field is activated, charges accumulate on the droplet side of the dielectric layer, forming
 167 a capacitor-like structure. This localized charge distribution results in a reduction of the
 168 interfacial energy near the contact line, thereby decreasing the apparent contact angle θ_{ED}
 169 of the droplet. The variation of the contact angle θ_{ED} with applied voltage is governed
 170 by the Young-Lippmann equation. To investigate the role of electric potential decay in
 171 electrowetting-induced wettability changes, we conduct droplet impact experiments at fixed
 172 dimensionless parameters, $Oh = 2.621 \times 10^{-3}$ and $Bo = 0.536$.

173 3.1. Phase Diagram and Classification of Electrowetting-Induced Wettability

174 When droplet impact the substrate with different electrowetting-induced wettability, it
 175 exhibits distinct dynamic reaction owing to voltage-induced variations in the equilibrium
 176 contact angle. Since the contact angle governs the balance of interfacial forces, the difference
 177 in wettability significantly influences the spreading, retraction, and rebound behaviour of
 178 the droplet. On a substrate with an equilibrium contact angle of 90° , the droplet follows the
 179 classical sequence of spreading, receding, and rebounding. At low impact velocities (i.e.,
 180 low Weber numbers), the droplet may remain entirely separated from the substrate by a
 181 thin air layer, resulting in non-contact bouncing. At sufficiently high Weber numbers, the

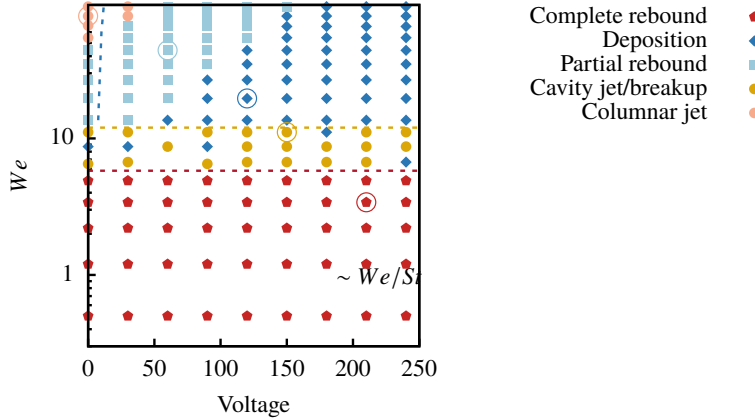


Figure 4: Phase diagrams of the motion state of a droplet impacting with the applied voltage varies obtained from simulations. Open-circle markers denote the selected cases corresponding to each regime.

182 droplet undergoes splashing, with the emission of secondary droplets. To systematically
 183 characterise the influence of electrowetting, we construct a phase diagram in the applied
 184 voltage-Weber number plane that delineates the regimes of droplet impact behaviour under
 185 varying wettability conditions. Figure 4 delineates the behavioural phase diagram of droplet
 186 impact regimes across applied voltages and Weber numbers, encompassing low-velocity
 187 complete rebound and cavity-induced jetting, alongside moderate-to-high-velocity partial
 188 rebound, deposition, and columnar liquid jetting regimes.

189 Figure 5 presents a morphological chronology of droplet evolution across distinct regimes,
 190 capturing the complete progression from initial contact to final configuration. Sequentially
 191 arranged are: columnar jetting, partial rebound, deposition, cavity-induced breakup, and
 192 complete rebound – corresponding to the phase diagram’s open-circle markers. Key fea-
 193 tures include central jet ejection (columnar jetting), necking phenomena (partial rebound),
 194 and filamentous jets (cavity regime/breakup), while deposition and complete rebound are
 195 distinguished by their final equilibrium states.

196 When a droplet impacts a solid wall at relatively high velocity, it typically exhibits
 197 splashing. For low-viscosity droplets, however, splashing behaviour is typically suppressed
 198 (Jian *et al.* 2018). Upon contacting the substrate, the droplet’s kinetic energy undergoes
 199 rapid conversion into surface energy. This process drives spreading to a maximum ra-
 200 dius. Subsequently, under the influence of significant surface energy potential, the droplet
 201 undergoes accelerated retraction. Capillary waves converging radially inwards from the
 202 spreading periphery focusing at the axisymmetric centre, thereby initiating vertical columnar
 203 jet formation. Figure 6 illustrates the droplet impact sequence from initial spreading
 204 through retraction to capillary wave convergence culminating in vertical liquid jet formation.
 205 Conversely, the cavity-jet/breakup regime manifests at low Weber numbers. Here, the air film
 206 at the droplet’s base remains intact throughout impact. During spreading, slow-propagating
 207 capillary waves converge centrally, generating an axial cavity. Subsequent accelerated
 208 retraction causes cavity collapse, inducing high-velocity jet ejection. This process typically
 209 culminates in extensive fragmentation due to vapour cavity implosion. Figure 7 delineates
 210 the complete evolution of central cavity formation through collapse-induced jetting. The
 211 implosion-driven jets exhibit elevated stagnation pressures, yielding ejected micro-droplets
 212 with enhanced velocities and reduced diameters.

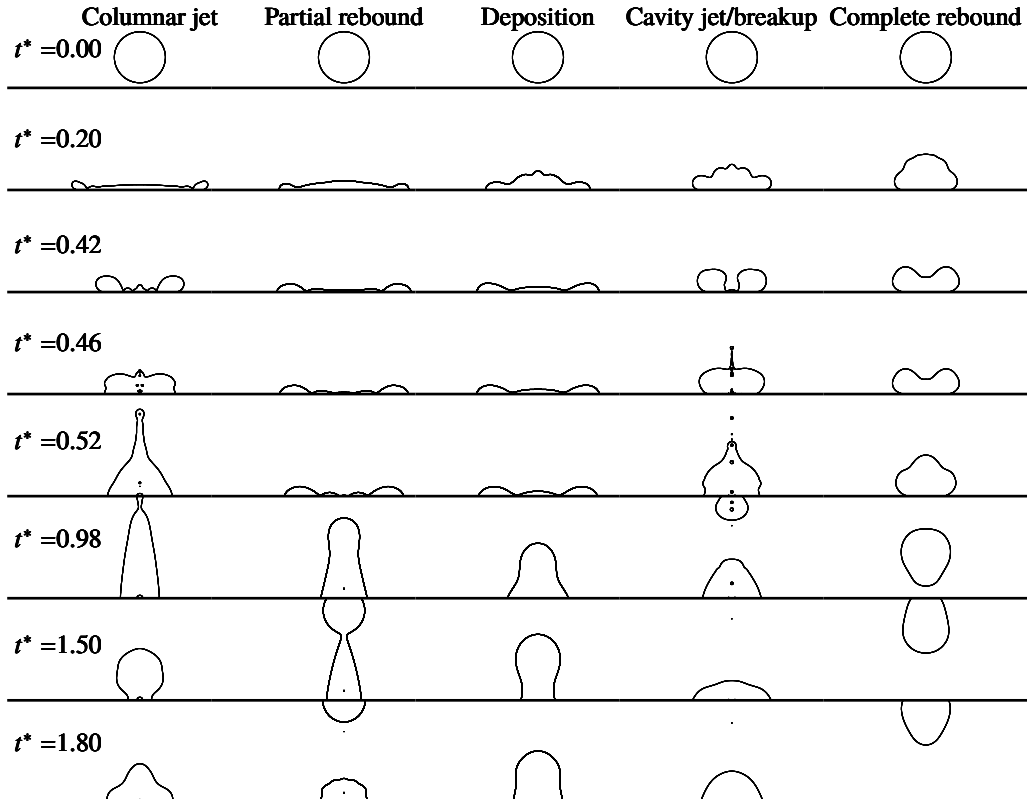


Figure 5: Phase diagrams of the motion state of a droplet impacting with the applied voltage varies obtained from simulations.

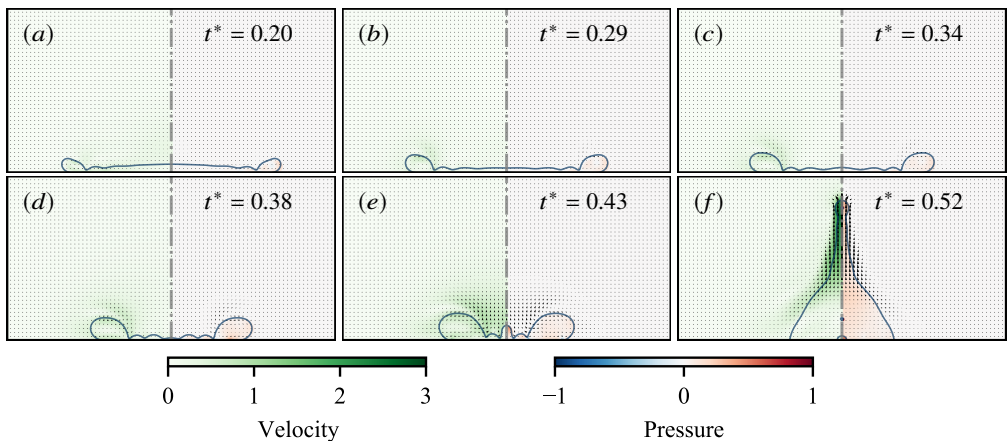


Figure 6: Phase diagrams of the motion state of a droplet impacting with the applied voltage varies obtained from simulations.

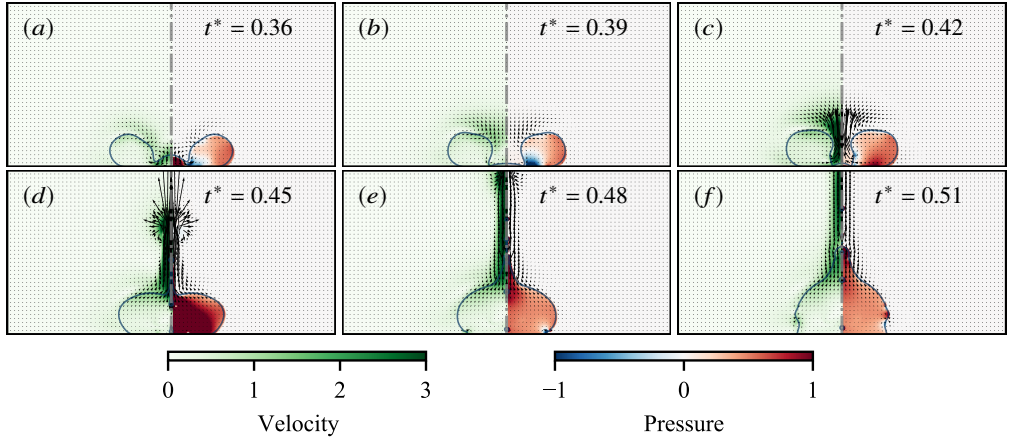


Figure 7: Phase diagrams of the motion state of a droplet impacting with the applied voltage varies obtained from simulations.

213 Within the moderate impact velocity regime, droplets typically achieve extensive spreading
 214 radii. Owing to substantial surface energy storage, accelerated retraction imparts sufficient
 215 kinetic energy to induce necking phenomena, ultimately enabling rebound detachment
 216 (partial rebound). In contrast, during deposition events, droplets possess insufficient kinetic
 217 energy upon impact. Significant viscous dissipation during spreading depletes momentum
 218 reserves, precluding rebound. Consequently, residual energy is exhausted through damped
 219 capillary-inertial oscillations until complete immobilisation (deposition).

220 To elucidate the energy evolution across the two regimes, we consider the total energy of
 221 the droplet and substrate system. The relevant energetic contributions are the kinetic energy
 222 E_k , the interfacial (capillary) energy E_γ , the electrostatic energy stored in the dielectric E_e ,
 223 the gravitational potential E_g (which may be negligible in the small-Bond-number limit),
 224 and the viscous dissipation E_d . The integrated energy balance between an initial time 0 and
 225 time t reads

$$226 \quad \Delta(E_k + E_g + E_\gamma + E_e) = -E_d + W_{\text{ext}}. \quad (3.1)$$

227 where W_{ext} denotes any external mechanical work (zero in the absence of external forcing).
 228 The electrostatic energy stored in the dielectric under the contact patch (parallel-plate
 229 approximation) is

$$230 \quad E_e(t) = \frac{1}{2} C(t) \phi^2 = \frac{1}{2} \frac{\epsilon_0 \epsilon_r A_{\text{SL}}(t)}{d} \phi^2, \quad (3.2)$$

231 where ϕ denotes the applied potential (constant-voltage case), d the dielectric thickness, and
 232 $A_{\text{SL}}(t)$ the instantaneous solid-liquid contact area.

233 It is often convenient to express the interfacial energy using Young's relation. Taking
 234 $\gamma_{\text{SG}} A_S$ as an arbitrary reference (constant) contribution and using $\gamma_{\text{LG}} \cos \theta_s = \gamma_{\text{SG}} - \gamma_{\text{SL}}$,
 235 the change in capillary energy relative to the reference can be written

$$236 \quad \Delta E_\gamma = \gamma_{\text{LG}} (A_{\text{LG}} - A_{\text{SL}} \cos \theta_s). \quad (3.3)$$

237 Under electrowetting 2.1 limit, if we compute the capillary energy using the voltage-
 238 dependent contact angle θ_{ew} ,

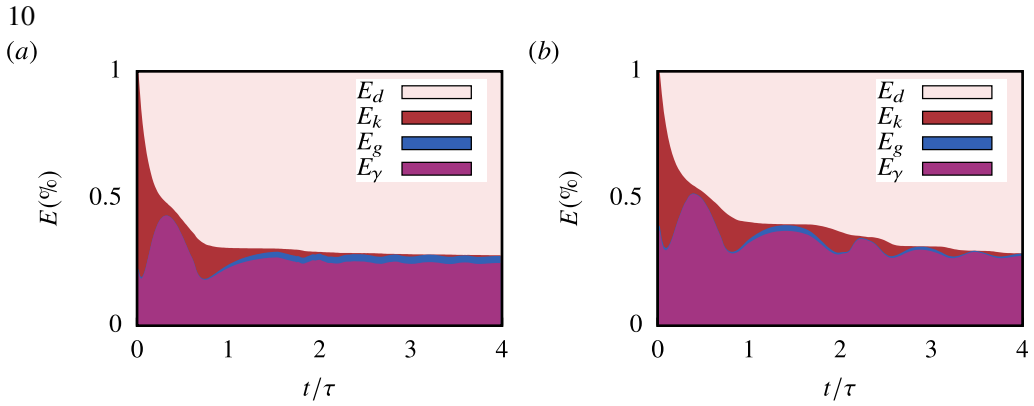


Figure 8: The energy transformations during the formation of (a) partial rebound, (b) deposition in the process of droplet impact on the substrate. The horizontal axis represents dimensionless time, and the vertical axis represents the distribution of the three energies.

239 $E_\gamma^{(\text{ew})} = \gamma_{\text{LG}}(A_{\text{LG}} - A_{\text{SL}} \cos \theta_{\text{ew}}), \quad (3.4)$

240 then substituting (2.1) yields the identity

241
$$E_\gamma^{(\text{ew})}(t) = \Delta E_\gamma(t) - \underbrace{\frac{\epsilon_0 \epsilon_r A_{\text{SL}}(t) \phi^2}{2d}}_{E_e(t)}. \quad (3.5)$$

242 Equation (3.5) demonstrates why we reduce the electrical term to the capillary energy.
243 Therefore, we write the global balance in the commonly used case with no external mechanical
244 work, the energy budget reduces to:

245
$$\Delta(E_k + E_g + E_\gamma^{(\text{ew})}) = -E_d. \quad (3.6)$$

246 Figure 12 delineates the temporal evolution of the energy budget for two regimes: partial
247 rebound (Fig. 12a) and deposition (Fig. 12b). The dynamics are predominantly governed by
248 the interplay and conversion between kinetic energy (E_k), surface energy (E_γ), and viscous
249 dissipation (E_d). In the case of partial rebound (Fig. 12a), the initial kinetic energy is rapidly
250 depleted during the early spreading stage ($t^* < 0.4$), being primarily converted into surface
251 energy to create a new liquid-gas interface and into energy dissipated through viscous effects.
252 The surface energy peaks concomitantly with the maximum spreading diameter. Crucially,
253 during the subsequent receding phase ($1.5 < t^* < 3.5$), a significant part of the stored surface
254 energy is converted back into kinetic energy, driving the recoil of the lamella and the uplift of
255 the central dome. However, the viscous dissipation E_d grows monotonically. This energy loss
256 ultimately inhibits full recoil, leaving the droplet in a partially rebounded equilibrium state.
257 The final morphology is thus a direct consequence of the balance between the recoverable
258 surface energy and the energy lost to dissipation.

259 Conversely, the energy history for the deposition case (Fig. 12b) reveals a distinctly
260 different pathway. While the initial conversion from kinetic to surface energy is similar, the
261 key distinction lies in the retraction stage. Here, the dissipation rate is significantly higher,
262 as evidenced by the steeper slope of E_d , often due to stronger interactions within fluid.
263 This heightened dissipation effectively arrests the retraction stage. The energy available for
264 recoil is insufficient to overcome the combined effects of surface adhesion. The surface
265 energy keeps at a relatively high value with a significant reconversion into kinetic energy.

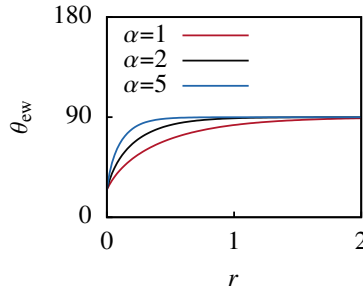


Figure 9: The energy transformations during the formation of (a) partial rebound, (b) deposition in the process of droplet impact on the substrate. The horizontal axis represents dimensionless time, and the vertical axis represents the distribution of the three energies.

Therefore, the droplet will oscillate up and down repeatedly on the ground until all its kinetic energy is exhausted, and settles into a stable, pancake-like deposited state. The energy budget demonstrates that deposition arises once viscous dissipation exhausts the droplet's kinetic energy and prevents the release of surface energy, effectively arresting the interface in a minimum surface energystate.

The state of Complete rebound is noticed to exist widely in the range of We number less than 5. The bouncing mechanism is predicated on the persistence of an air film sustained at low impact velocities. This sub-micrometre air cushion dissipates kinetic energy and reverses the momentum of droplets. Consequently, the interposition of the air film prevents direct contact between the droplet and substrate during low-velocity impact; thereby eliminating wettability-dependent effects. As this mechanism has been extensively documented in prior studies, it is not the primary focus of the present analysis.

3.2. Influence of Electric Potential Decay on Droplet Behavior

Incorporating a voltage attenuation coefficient into this model induces profound alterations in droplet dynamics. Modifying the α -parameter in Equation 2.12 drastically perturbs the interfacial voltage distribution. Consequently, the formerly uniform solid-liquid contact angle is supplanted by a conical distribution-minimised centrally and maximised peripherally-owing to voltage decay.

3.3. Frequency-Dependent Response of Electrowetting-Induced Motion

4. Conclusion

Funding. This research was supported in part by the National Natural Science Foundation of China (No. 11972170).

Declaration of interests. The authors report no conflict of interest.

Author ORCIDs. Authors may include the ORCID identifiers as follows. Ziqiang Ma, <https://orcid.org/0000-0003-3608-0199>; Xinping Zhou, <https://orcid.org/0000-0001-6340-5273>

REFERENCES

- AFKHAMI, S., BUONGIORNO, J., GUION, A., POPINET, S., SAADE, Y., SCARDOVELLI, R. & ZALESKI, S. 2018 Transition in a numerical model of contact line dynamics and forced dewetting. *J. Comput. Phys.* **374**, 1061–1093.
- AFKHAMI, S., ZALESKI, S. & BUSSMANN, M. 2009 A mesh-dependent model for applying dynamic contact angles to VOF simulations. *J. Comput. Phys.* **228** (15), 5370–5389.

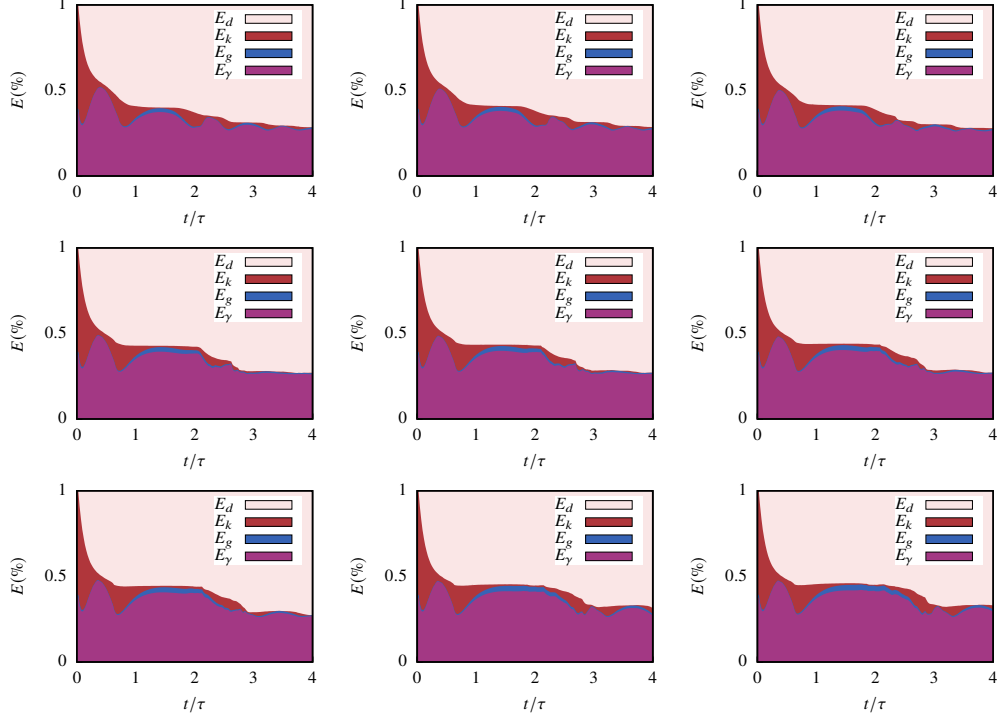


Figure 10: The energy transformations during the formation of (a) partial rebound, (b) deposition in the process of droplet impact on the substrate. The horizontal axis represents dimensionless time, and the vertical axis represents the distribution of the three energies.

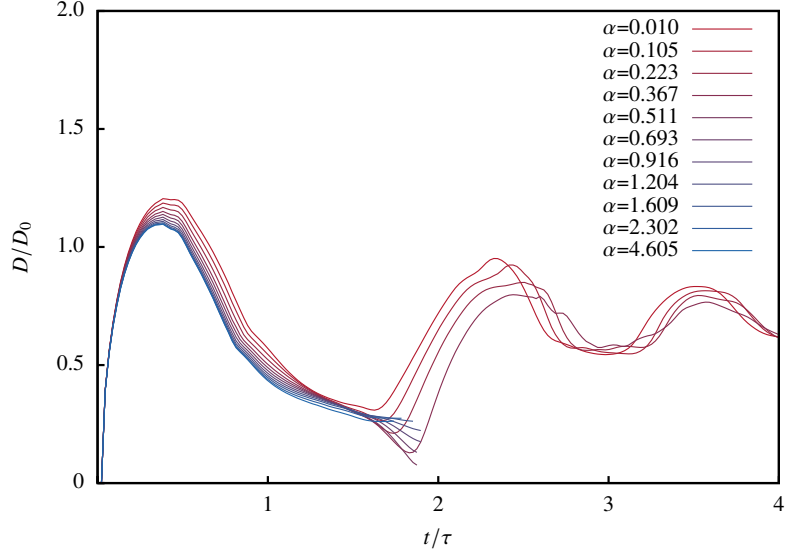


Figure 11: The energy transformations during the formation of (a) partial rebound, (b) deposition in the process of droplet impact on the substrate. The horizontal axis represents dimensionless time, and the vertical axis represents the distribution of the three energies.

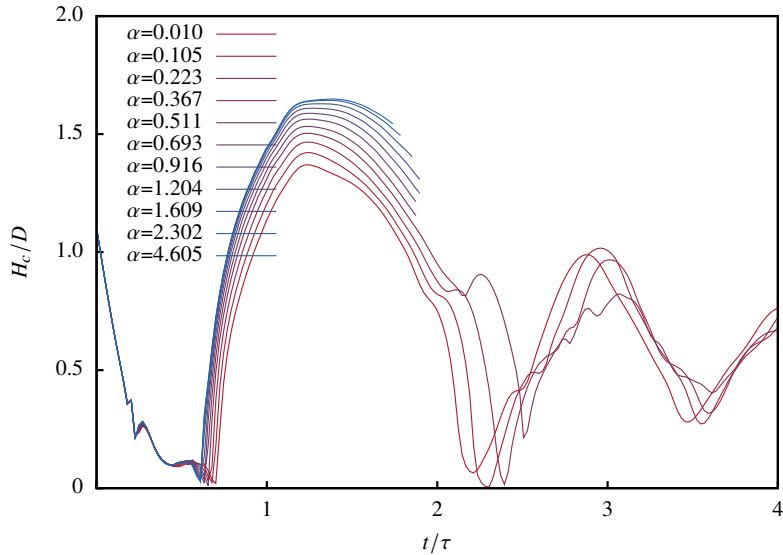


Figure 12: The energy transformations during the formation of (a) partial rebound, (b) deposition in the process of droplet impact on the substrate. The horizontal axis represents dimensionless time, and the vertical axis represents the distribution of the three energies.

- 296 CHENG, Y., WANG, F., XU, J., LIU, D. & SUI, Y. 2018 Numerical investigation of droplet spreading and heat
297 transfer on hot substrates. *International Journal of Heat and Mass Transfer* **121**, 402–411.
298 DUVIVIER, D., BLAKE, T.D. & DE CONINCK, J. 2013 Toward a predictive theory of wetting dynamics.
299 *Langmuir* **29** (32), 10132–10140.
300 JIAN, Z., JOSSERAND, C., POPINET, S., RAY, P. & ZALESKI, S. 2018 Two mechanisms of droplet splashing on
301 a solid substrate. *Journal of Fluid Mechanics* **835**, 1065–1086.
302 KOROBKIN, A.A., ELLIS, A.S. & SMITH, F.T. 2008 Trapping of air in impact between a body and shallow
303 water. *J. Fluid Mech.* **611**, 365–394.
304 KUMAR, A. & PATHAK, M. 2024 Droplet impact characteristics on hydrophobic surfaces with partial
305 electrowetting effects. *Physics of Fluids* **36** (9), 092126.
306 LI, E.Q. & THORODDSEN, S.T. 2015 Time-resolved imaging of a compressible air disc under a drop impacting
307 on a solid surface. *J. Fluid Mech.* **780**, 636–648.
308 MANDRE, S., MANI, M. & BRENNER, M.P. 2009 Precursors to Splashing of Liquid Droplets on a Solid
309 Surface. *Phys. Rev. Lett.* **102** (13), 134502.
310 POPINET, S. 2003 Gerris: a tree-based adaptive solver for the incompressible euler equations in complex
311 geometries. *J. Comput. Phys.* **190** (2), 572–600.
312 POPINET, S. 2009 An accurate adaptive solver for surface-tension-driven interfacial flows. *J. Comput. Phys.*
313 **228** (16), 5838–5866.
314 SMITH, F.T., LI, L. & WU, G.X. 2003 Air cushioning with a lubrication/inviscid balance. *J. Fluid Mech.* **482**,
315 291–318.
316 ŠIKALO, V., MARENKO, M., TROPEA, C. & GANIĆ, E.N. 2002 Analysis of impact of droplets on horizontal
317 surfaces. *Experimental Thermal and Fluid Science* **25** (7), 503–510.